Magnetic and optical properties of Fe doped crednerite CuMnO$_2$

Kaushal K. Shukla,[a] P. Shahi,[a] Gopal S.,[b] A. Kumar,[a] A. K. Ghosh,[c] Ripandeep Singh,[d] Neetika Sharma,[d] A. Das,[d] A. K. Sinha,[e] Amish G. Joshi,[f] A. K. Nigam[g] and Sandip Chatterjee*[a]

A geometrically frustrated magnetic CuMnO$_2$ system has been investigated because of its rich magnetic properties. Neutron diffraction, synchrotron X-ray, magnetic, X-ray photoemission spectroscopy (XPS) and UV-Visible spectroscopy measurements have been carried out on CuMnO$_2$ and 5% Fe doped CuMnO$_2$ samples. Fe doping reduces the distortion. Moreover, Fe doping induces the ferromagnetic coupling between *ab* planes. The value of magnetization is increased with Fe doping but coercivity is decreased. These might be due to the direct Mn–Mn exchange and Mn–O–Cu–O–Mn super–super exchange interactions. The UV-Vis data indicate the appearance of new energy bands in these compounds. The XPS study indicates that Fe is in the 3+ state.

Introduction

Geometrically frustrated magnetic systems have attracted much attention due to their interesting magnetic properties.[1–3] In these systems, spin ordering is suppressed by competing exchange interactions well below the Curie temperature. ABO_2-type triangular-lattice antiferromagnets in which not all the interactions are minimized simultaneously, are popular examples of geometrically frustrated systems.[4–7] Crednerite CuMnO$_2$ is an ABO_2-type triangular-lattice antiferromagnet. The crystal structure of CuMnO$_2$ contains of isosceles-triangular lattices of Mn. It has a monoclinic structure with $C2/m$ space group; it is distorted from the hexagonal delafossite structure because of Jahn–Teller effect of Mn^{3+} ions that have crystal-field splitting in e$_g$ orbitals due to d^4 electronic configuration. Moreover, different directions in the triangular *ab* plane become inequivalent: for each Mn, two short and four long Mn–Mn distances exist. It is observed that the exchange interaction at short bonds is stronger, which, with the uniaxial magnetic anisotropy of Mn^{3+} (spins are oriented predominantly along the long Mn–O bonds), leaves the system frustrated. This degeneracy is lifted below magnetic transition:

at $T < T_N = 65$ K and the structure changes from monoclinic to triclinic (space group $C1$) due to magnetostriction.[8] Recently, Ushakov *et al.* have shown that the presence of ferro-orbital ordering in Cu$_{1+x}$Mn$_{1-x}$O$_2$ plays a very important role in determining the exchange constants and the magnetic structure.[9]

Furthermore, in nonstoichiometric crednerite with a small excess of copper (Cu$_{1.04}$Mn$_{0.96}$O$_2$), the in plane magnetic ordering remains practically the same as for pure CuMnO$_2$, the interlayer exchange coupling changes from antiferromagnetic in CuMnO$_2$ to ferromagnetic in Cu$_{1.04}$Mn$_{0.96}$O$_2$ and *vice versa*.[10] Recent neutron diffraction studies have revealed the magnetic structure of CuMnO$_2$ and the crystal structure deformation associated with the magnetic ordering.[8,11] The magnetic structure below $T_N = 65$ K is the collinear one with the magnetic propagation vector $\boldsymbol{k}_1 = (1/2 \cdot 1/2 \cdot 1/2)$. In addition to $\boldsymbol{k}_1$, they observed the other group of the magnetic Bragg reflections which are assigned by $\boldsymbol{k}_2 = (1/2 \cdot 1/2 \cdot 0)$. While the intensity for $\boldsymbol{k}_1$ is dominant, that for $\boldsymbol{k}_2$ is speculated to be caused by a small amount of impurity of Cu$_{1+x}$Mn$_{1-x}$O$_2$.[8] Trari *et al.*[12] reported the magnetic susceptibility of Cu$_{1+x}$Mn$_{1-x}$O$_2$ (with $x = 0$–0.2), suggesting that the magnetic susceptibility is highly sensitive to the atomic disorders. However, the minor fraction for $\boldsymbol{k}_2$ has not been investigated thus far. The structural phase transition also occurs below T_N from the monoclinic $C2/m$ to the triclinic $C\bar{1}$ in CuMnO$_2$.[8,11] The degeneracy in the exchange interaction paths between base sites and apex sites in isosceles triangular lattice, J_2, is lifted by the distortion. It is evident from these previous studies that interlayer coupling plays a significant role in the long range magnetic ordering in CuMnO$_2$, and that this can be characterised using neutron diffraction. There is some dispute, however, over the source of the $\boldsymbol{k}_2$ ordering as to whether it is intrinsic to the structure or a result of some impurity. In this study, we have thus

[a]Department of Physics, Indian Institute of Technology (Banaras Hindu University), Varanasi-221005, India. E-mail: schatterji.app@iitbhu.ac.in

[b]School of Material Science & Technology, Indian Institute of Technology, (Banaras Hindu University), Varanasi 221005, India

[c]Department of Physics, Banaras Hindu University, Varanasi 221005, India

[d]Solid State Physics Division, Bhabha Atomic Research Centre, Mumbai 400085, India

[e]Indus Synchrotrons Utilization Division, Raja Ramanna Centre for Advanced Technology, Indore 452013, India

[f]CSIR-National Physical laboratory, Dr. K.S. Krishnan Road, New Delhi 110 012, India

[g]Department of CMP & MS Tata Institute of Fundamental Research, Mumbai, 400005, India

doped Fe into the Mn site in $CuMnO_2$ so as to examine the effects on the inter-layer coupling and on this ordering.

Experimental

The $CuMn_{1-x}Fe_xO_2$ (with $x = 0.0$ and 0.05) samples were prepared by solid state reaction in an evacuated quartz tube. Powders CuO, MnO and Fe_2O_3 were mixed in appropriate ratio and pressed into pellets. The pellets were then placed in an alumina crucible, sealed in quartz tube under high vacuum ($\sim 10^{-6}$ mbar) and heated at 950 °C for 12 h. Powder XRD data were recorded using ADXRD beam line (on bending magnet port BL-12) of the Indus-2 (2.5 GeV, 100 mA) synchrotron radiation (SR) source at Raja Ramanna Centre for Advanced Technology (RRCAT), Indore, India. The diffraction data were collected on a image plate (mar 345) detector. The diffraction images were integrated using FIT2D program. Wave length and sample to detector distance were accurately calibrated using XRD pattern of LaB_6 NIST standard. Neutron powder diffraction (NPD) patterns were recorded on the PD2 diffractometer ($\lambda = 1.2443$ Å) at Bhabha Atomic Research Centre, Mumbai, India. The observed XRD and neutron powder diffraction patterns were analyzed by Rietveld method using the Fullprof-2K software package. The basis vector for the magnetic refinement was determined using BASIREPS program. Magnetic measurements were carried out using MPMS, SQUID (Quantum Design) magnetometer with the bulk samples. Data were collected during warm up cycle. The absorption spectra were measured in the range of 200–800 nm using UV-Vis spectrometer. X-ray Photoelectron Spectroscopy (XPS) experiments were performed using Omicron Nanotechnology UHV system equipped with a twin anode Mg/Al X-ray source (DAR400), a monochromatic source (XM 1000) and a hemispherical electron energy analyzer (EA125). All the XPS measurements were performed inside the analysis chamber under average base vacuum of 8.1×10^{-10} Torr using monochromatized $AlK\alpha$ at 15 kV and 300 watt. The total energy resolution, estimated from the width of the Fermi energy, was about 250 meV for monochromatic $AlK\alpha$ line with photon energy 1486.7 eV. During photoemission studies, small specimen charging was observed which was later calibrated by assigning the C1s signal at 284.6 eV. Resistivity measurements have been performed by four probe method.

Results and discussions

Structural characterization

The results of the refinements using Synchrotron X-ray diffraction data and neutron diffraction data are shown in Fig. 1 and 2 (room temperature), and Tables 1 and 2, respectively. These show good agreement with previously reported data for the crednerite structure of $CuMnO_2$.[13,14] The cell volume of $CuMn_{0.95}Fe_{0.05}O_2$ (92.1062 Å^3) is slightly larger than that of $CuMnO_2$ (91.9023 Å^3); it corresponds mainly to a decrease of a, an increase of the β angle, and a small increase of b and c. The changes in the β angle, a and b parameters will have effects on the exchange interactions between ab planes and in the basal plane, respectively. In the same way, the dilution on the Mn site,

because of the small substitution of Fe for Mn, induces a smaller (Mn/Fe–O) average distance 2.0446(3) Å compared to 2.0451(5) Å for $CuMnO_2$ and a smaller Jahn–Teller distortion of the MnO_6 octahedra (by comparing the $\delta = d(Mn–O)apical/d(Mn–O)equatorial$). The irregularity in the triangular Mn lattice in the basal plane also increases very slightly with the shortest Mn–Mn distance (2.8877(3) Å) which is slightly longer than in $CuMnO_2$ (2.8876(8) Å) and also the two longest distances (3.1532(1) Å) are larger than in $CuMnO_2$ (3.1531(5) Å). At room temperature, the Cu–O distances also slightly vary by the substitution, close to 1.8392(5) Å in $CuMnO_2$ and to 1.8470(1) Å in $CuMn_{0.95}Fe_{0.05}O_2$.

We have also measured the neutron diffraction at 6 K for both $CuMnO_2$ and $CuMn_{0.95}Fe_{0.05}O_2$. In Fig. 3 we have shown the neutron diffraction pattern of $CuMn_{0.95}Fe_{0.05}O_2$. On lowering the sample temperature superlattice reflections in both these compounds are observed indicating the antiferromagnetic nature of these compounds. On lowering of temperature we do not observe the splitting of the (220) reflection (the splitting of which indicates the transition from monoclinic to triclinic structure).[15] A marginal improvement in the fit is obtained in the triclinic phase but we have analysed the diffraction in the monoclinic structure in $C2/m$ space group at 6 K. The cell parameters of Fe doped $CuMnO_2$ ($a = 5.5582(4)$ Å, $b = 2.8850(2)$ Å, $c = 5.8986(4)$ Å, $\beta = 104.230(7)$), significantly differ from those of $CuMnO_2$ ($a = 5.5675(5)$ Å, $b = 2.8759(2)$ Å, $c = 5.8811(5)$ Å, $\beta = 104.058(1)$). Compared to RT, the difference in the cell volume is more at low temperature (LT) in Fe doped $CuMnO_2$. In this low temperature structure, the oxygen atoms occupy a general symmetry lattice site (x, y, z) and the oxygen position at low temperature also varies with Fe doping. Dealing with the triangular Mn-array in the (a, b) plane, the Mn–Mn shortest edge of the triangle is slightly elongated (from 2.8759 Å along [010] to 2.8850 Å along [110]). In the MnO_6 octahedron at low temperature, the two long apical Mn–O distances are 2.2574 Å, while the four equatorial distances are (1.9278 Å). While, for $CuMnO_2$ in the MnO_6 octahedron at low temperature, the apical Mn–O distances are 2.2618 Å, and the equatorial distances are 1.9277 Å indicating that Fe doping decreases the distortion in MnO_6 octahedra. For nonstoichiometric $Cu_{1.04}Mn_{0.96}O_2$ sample also the distortion in MnO_6 octahedra is decreased.[10] Therefore, no change in the chemical structure is
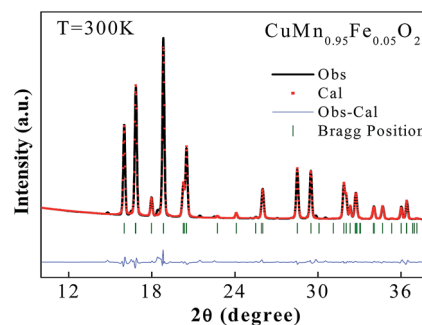

Fig. 1 Rietveld refinement of synchrotron X-ray powder diffraction data of $CuMn_{0.95}Fe_{0.05}O_2$ at room temperature.
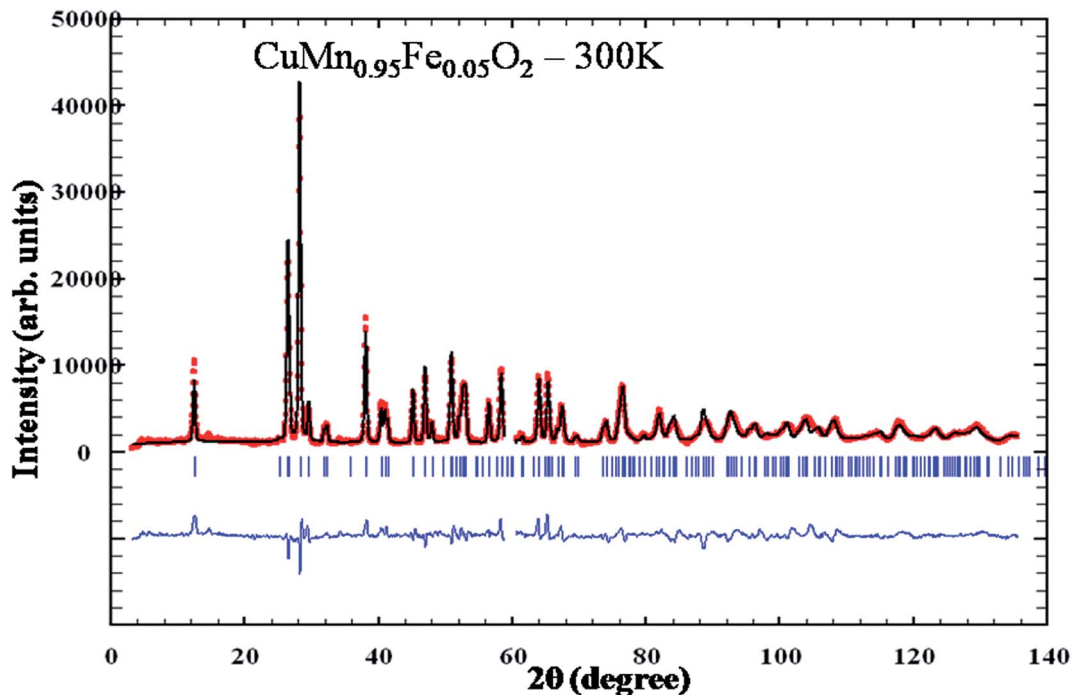
Fig. 2 Rietveld refinement of neutron powder diffraction data of $CuMn_{0.95}Fe_{0.05}O_2$ at room temperature.

observed on Fe doping, although the magnetic structure is found to be different on Fe doping. The structural parameters obtained from the analysis are summarized in Table 1. In the

Table 1 Rietveld refinement of room temperature synchrotron XRD of $CuMnO_2$ and $CuMn_{0.95}Fe_{0.05}O_2$

Sample/parameters	$CuMnO_2$, 300 K	$CuMn_{0.95}Fe_{0.05}O_2$, 300 K
Space group	$C2/m$	$C2/m$
Cell parameters		
a (Å)	5.6063(3)	5.6064(3)
b (Å)	2.8876(8)	2.8877(3)
c (Å)	5.8990(3)	5.8990(3)
Cell volume (Å)^3	92.6774	92.6823
α (deg)	90	90
β (deg)	103.965(3)	103.961(3)
γ (deg)	90	90
Atomic positions		
O(4i)x	0.4073	0.39978
y	0	0
z	0.17890	0.17789
Occupancy		
Cu	1	1
Mn	1	0.95
Fe		0.05
Mn–Mn	2.8876(8) × 2	2.8877(3) × 2
	3.1531(5) × 4	3.1532(1) × 4
Cu–O	1.8392(5) × 2	1.8470(1) × 2
Bragg R factor	4.139	2.886
R_F	2.601	2.101
R_P	9.70	8.07
R_{wp}	10.09	9.72
X^2	2.44	1.98

case of $CuMnO_2$ the superlattice reflections were indexed using the two propagation vectors $k_1 = (1/2 \cdot 1/2 \cdot 1/2)$ and $k_2 = (1/2 \cdot 1/2 \cdot 0)$. The intensities corresponding to k_2 were very weak in agreement with Damay et al.,[8] but not absent as reported previously in this compound.[16] The magnetic structure described by k_1 consists of antiferromagnetic chains in the (a, b) plane coupled antiferromagnetically along the c-axis. The components of the moment are 3.2 μ_B and 1.9 μ_B along a and c-axes corresponding to 3.3 μ_B. For k_2 vector the magnetic

Table 2 Rietveld refinement of the neutron powder diffraction data for $CuMnO_2$ and $CuMn_{0.95}Fe_{0.05}O_2$ at 6 K

Sample/parameters	$CuMnO_2$, 6 K	$CuMn_{0.95}Fe_{0.05}O_2$, 6 K
Space group	$C2/m$	$C2/m$
Cell parameter		
a (Å)	5.5675(5)	5.5582(4)
b (Å)	2.8759(2)	2.8850(2)
c (Å)	5.8811(5)	5.8986(4)
Cell volume (Å)^3	91.3454	91.6842
α (deg)	90	90
β (deg)	104.058	104.230(7)
γ (deg)	90	90
Atomic positions		
O(4i)x	0.4081(5)	0.4087(5)
y	0	0
z	0.1802(4)	0.1790(4)
Mn–O'	2.2618(×2)	2.2574(×2)
Mn–O''	1.9277(×4)	1.9278(×4)
Mn–Mn	3.1332(×4)	3.1312(×4)
	2.8759(×2)	2.8850(×2)

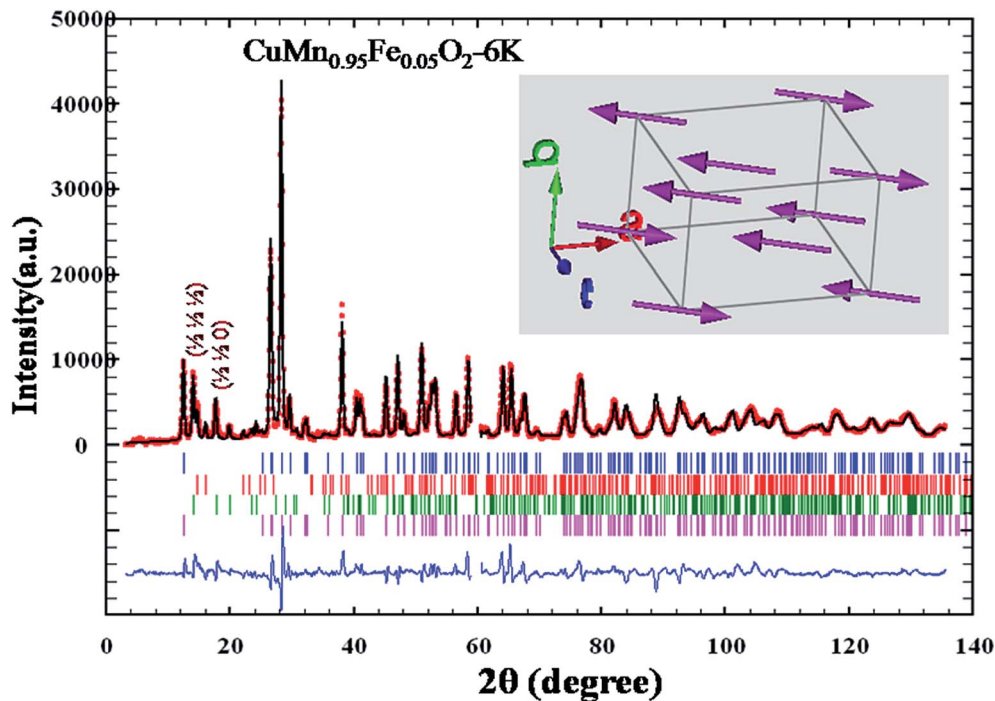**Fig. 3** Rietveld refinement of neutron powder diffraction data of $CuMn_{0.95}Fe_{0.05}O_2$ at 6 K.

moment is 0.9(3) μ_B and oriented along *c*-axis. The total moment is lower than the expected moment of 4 μ_B for Mn^{3+} in high spin state. Fe is found to substitute at the Mn site. It results in a large increase in the intensity of $(1/2 \cdot 1/2 \cdot 0)$ reflection corresponding to $\mathbf{k}_2$. The moment oriented along *a* and *c* are 2.4 μ_B and 2.0 μ_B, respectively leading to a total moment of 2.7 μ_B. The moment corresponding to $\mathbf{k}_1$ vector is 1.8 μ_B. A net increase in the moment (4.5 μ_B) is observed as expected for a mixture of Mn^{3+} (4 μ_B) and Fe^{3+} (5 μ_B), which is nearly equal to the saturation value of the $Cu(Mn, Fe)O_2$ sample. The appearance of $\mathbf{k}_2$ propagation vector indicates the ferromagnetic coupling between *ab* planes.

Optical properties

We have also studied the electronic structure of $CuMnO_2$ and $CuMn_{0.95}Fe_{0.05}O_2$ using X-ray photoemission spectroscopy (XPS). The purpose of this study was to investigate any role of the electronic structure on the magnetic properties of $CuMnO_2$. The XPS core level spectra of Cu2p, Mn2p and Fe2p and O1s are shown in Fig. 4(a–d). Fig. 4(a) shows high resolution spectra of Cu2p core level. Two clear distinct states of $Cu(2p_{3/2})$ at 952 eV and $Cu(2p_{1/2})$ at 932 eV are separated by 19.75 eV and 19.9 eV for $CuMnO_2$ and $CuMn_{0.95}Fe_{0.05}O_2$, respectively. Fig. 4(b) shows core level spectra of Mn2p. Two separate states of $Mn(2p_{3/2})$ and $Mn(2p_{1/2})$ observed at 641.6 eV and 652.95 eV for $CuMnO_2$ and 641.3 eV and 652.9 eV for $CuMn_{0.95}Fe_{0.05}O_2$, respectively. Fig. 4(c) exhibit Fe2p core level spectra of $CuMn_{0.95}Fe_{0.05}O_2$ compound which shows the spin–orbit splitting of the Fe2p level, manifested as $Fe2p_{3/2}$ and $Fe2p_{1/2}$. The difference between these two Fe peaks is 13.5 eV, which confirms the presence of

Fe^{3+} state. These observed doubly states are due to the spin–orbit coupling. Slight shifting in the states with Fe doping occurs due to change in interaction energy between Cu and transition metal ion. These data clearly suggest that Cu is in +1 state and both Mn and Fe are in +3 state. Fig. 4(d) shows the spectra of oxygen which has two peak structures. Two peaks marked as X observed at 529.8 eV and 529.6 eV and Y at 531.55 eV and 531.1 eV for $CuMnO_2$ and $CuMn_{0.95}Fe_{0.05}O_2$, respectively. The first peak marked as X, is characteristic peak of "O^{2-}" ions of the lattice oxygen, while peak Y denotes O(1s) lateral structure. This lateral peak corresponds to the ionizations of weakly adsorbed species[17] and also the ionizations of oxygen ions with particular coordinates, more specifically integrated in the subsurface. This suggests that the existence, in the subsurface of oxygen ions that bear lower electron density than the "O^{2-}" ions. Normally, these oxide ions can be described as "O^-" species or excess oxygen. When the density of lattice oxygen varies, the area ratio of these two peaks *i.e.* X and Y also changes. Valence level spectra of $CuMnO_2$ and $CuMn_{0.95}Fe_{0.05}$-O_2 samples are shown in Fig. 5. Four features (A, B, C, D) can be identified in the experimental spectra of both the samples. Feature A relate to state of dominant Cu3d atomic character while B and C relate to the hybridization with Cu3d and Mn3d to O2p.[18] Feature D is a tail like structure near the Fermi level, E_F. The electronic states near the Fermi level are mostly responsible for the electronic properties. A comparison of the valence band spectra for the two samples reveals that the density of states is negligibly small but finite at E_F which is clear from the inset of Fig. 5. The density of states slightly increases with Fe doping. Therefore, conductivity increases slightly with Fe doping. The XRD and neutron diffraction data also support
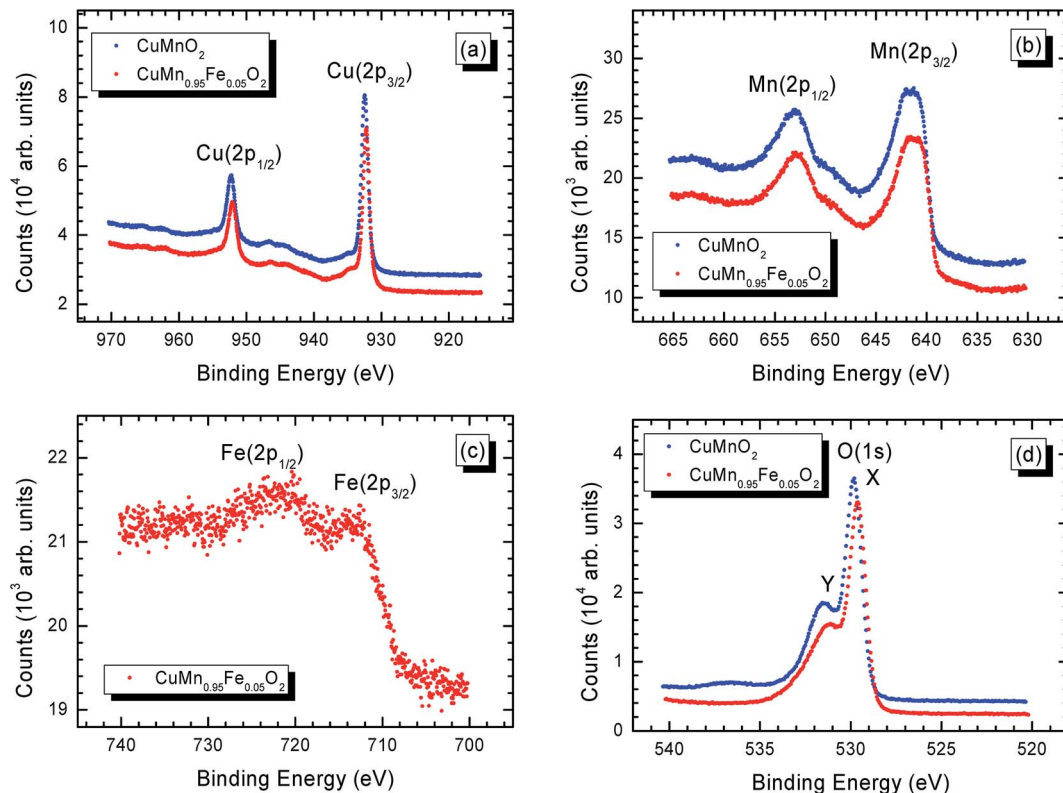
Fig. 4 XPS core level spectra of (a) Cu2p (b) Mn2p (c) Fe2p and (d) O1s [(●) blue dots for CuMnO$_2$ and red dots (●) for CuMn$_{0.95}$Fe$_{0.05}$O$_2$].

this. It is observed from Table 1 that on Fe doping Cu–O bond length increases and Mn–O bond length decreases. This will lead to the increase of bandwidth and as a consequence band gap will decrease.[18] Moreover, it has been observed (Table 1) that on Fe doping the c axis is elongated leading to weaker Cu3d–O2p hybridization. In the valence band spectra (Fig. 5) also it is found that in CuMn$_{0.95}$Fe$_{0.05}$O$_2$ the B and C features are reduced with respect to the A feature in accordance with the XRD and neutron diffraction data (Table 1). It is worthwhile to mention that the valence band spectrum of CuMnO$_2$ differs from that of CuCrO$_2$ (ref. 19) in respect of non-existence of the shoulder at the upper part of the valence band indicating that Mn3d is located away from the Fermi level. The most interesting feature is the shift of Fermi level towards lower binding energy for both CuMnO$_2$ and CuMn$_{0.95}$Fe$_{0.05}$O$_2$ unlike CuCrO$_2$.[18,19] Similar behavior is observed in K doped SrCu$_2$O$_2$.[20] This shift is related to low activation energy of CuMnO$_2$. Furthermore, with Fe doping it is observed that shift in Fermi energy is slightly larger than that in undoped sample. This is close to the further change in activation energy. Therefore, the photo emission spectroscopy measurements confirm the movement of Fermi level towards the valence band edge on Fe doping which is accompanied by corresponding shifts in core level binding energies. Similar kind of movement is observed in CuCrO$_2$ with Mg doping.[20] In the present investigation the Cu2p$_{3/2}$ peak shifts with Fe doping from 932.45 eV to 932.2 eV.

The absorption curves of CuMnO$_2$ and Fe doped CuMnO$_2$ are shown in Fig. 6. As the photon energy increases the absorption

intensity increases and attains a maximum. For the undoped sample the maximum occurs at E = 4.2 eV whereas for the Fe doped sample it increases to 4.5 eV. The peak can be assigned to
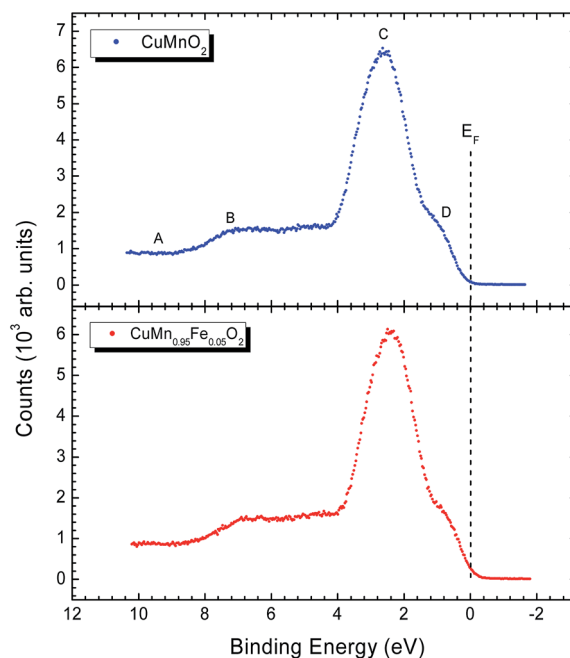

Fig. 5 Valance-band XPS spectra of CuMnO$_2$ and CuMn$_{0.95}$Fe$_{0.05}$O$_2$ [(●) blue dots for CuMnO$_2$ and red dots (●) for CuMn$_{0.95}$Fe$_{0.05}$O$_2$].

an excitonic excitation from Cu3d + O2p to Cu3d + 4s.[19,20] For the Fe doped sample the peak intensity becomes negligibly small, the reason of which is not yet clear. It deserves further study. Moreover, the optical band gaps result from the relationship between the optical absorption coefficient and the photon energy ($h\nu$) can be expressed as:

$$(\alpha h\nu)^2 = A(h\nu - E_g)$$

where A is a constant and E_g is the direct optical band gap of the material. The inset of Fig. 6 shows the optical band gap of the undoped and Fe doped $CuMnO_2$. It is observed from the figure that both samples have two energy band gaps. The band gaps of the crednerite $CuMnO_2$ (4.60 eV and 4.90 eV) and $CuMn_{0.95}Fe_{0.05}O_2$ (4.60 eV and 4.79 eV) are close to each other. Therefore, for both the samples an additional energy level exists near the valence band edge, as also revealed by valence band spectra (Fig. 5). The difference between the new band and the conduction band is 4.60 eV for both the samples. On the other hand, the new band resides 0.30 eV and 0.19 eV above the top of the valence band respectively for $CuMnO_2$ and $CuMn_{0.95}Fe_{0.05}O_2$. Similar, new band is observed in $CuGa_{0.8}Cr_{0.2}O_2$ film.[21] Appearance of new band might be the reason of the shifting of Fermi level towards the valence band edge observed in valence band spectra (Fig. 5). Moreover, observed band gaps of these systems come in the range of wide band gap semiconductors and these values are even more than the band gap of ZnO (3.37 eV) and GaN (3.44 eV).[22–24] Additionally, these systems show much better magnetic ordering and magnetic moment than any known diluted magnetic semiconductors, which might prove significant in the application of these materials as magnetic semiconductors.

Electrical properties

In order to understand the intrinsic characteristic, we have also studied the temperature dependence of resistivity for both $CuMnO_2$ and $CuMn_{0.95}Fe_{0.05}O_2$ compounds. The exponential decrease in resistivity with the increase in temperature indicates the semiconducting nature of both the samples. The plot of ln ρ versus 1000/T (Fig. 7) shows that thermally activated band co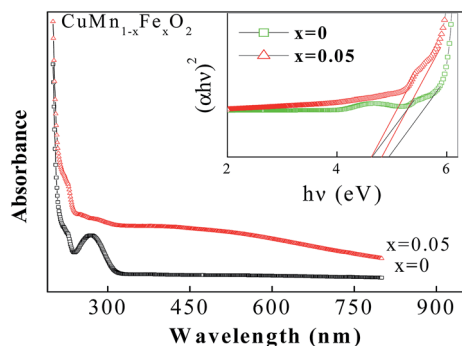nduction is the dominant mechanism at high-temperature region. The thermally activated resistivity at high-temperature region follows the Arrhenius law

$$\rho(T) = \rho_0 \exp[E_a/k_B T] \tag{1}$$

where k_B is the Boltzmann's constant and E_a is the activation energy. The deviation from the linear fit indicates that thermal activation mechanism is not valid at lower temperature region. The variable-range-hopping (VRH) conduction of polarons has been found to dominate in this temperature region. The conduction mechanism due to the variable range hopping of polaron at low temperature can be described by the Mott's equation[25]

$$\rho(T) = \rho_0 \exp[T_0/T]^{1/4} \tag{2}$$

where ρ_0 and T_0 are constants and are given by $\rho_0 = \{[8\pi\alpha k_B T/N(E_F)]^{1/2}\}/(3e^2\nu_{ph})$ and $T_0 = 18\alpha^3/[kN(E_F)]$ where ν_{ph} ($\sim 10^{13}$ s^{-1}) is the phonon frequency at Debye temperature, $N(E_F)$ is the density of localized electron states at the Fermi level, and α is the inverse localization length. For $CuMnO_2$ two slopes are observed which can be fitted with the eqn (1). The estimated activation energy (E_a) from the two slopes are 0.29 eV and 0.96 eV. The estimated activation energy (E_a) for $CuMn_{0.95}Fe_{0.05}O_2$ using Arrhenius law is 0.90 eV. Moreover, we did not get proper fitting with the eqn (2).

Magnetic properties

Fig. 8 shows the magnetization of $CuMnO_2$ as a function of magnetic field. At 5 K, a clear hysteresis with a coercive field of 2.46 kOe is observed. The magnetization increases almost linearly with magnetic field after closing of the hysteresis. The magnetic properties of $CuMnO_2$ are controversial.[26,27] Our data match with the data in ref. 19. The data indicate the presence of the dominating AFM order with some FM ordering. The AFM
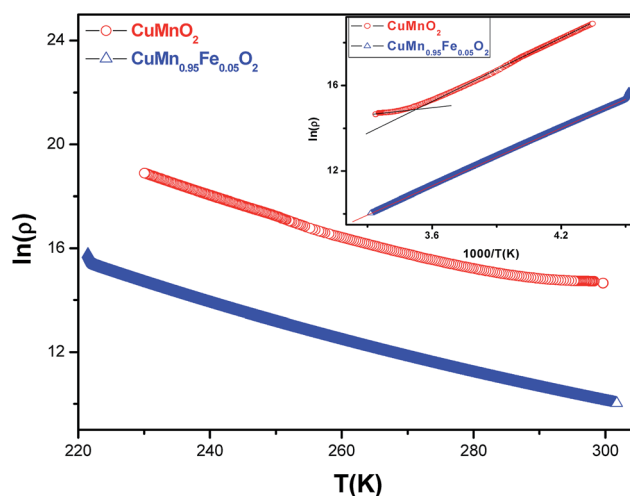
Fig. 6 Absorption spectra of $CuMnO_2$ and $CuMn_{0.95}Fe_{0.05}O_2$. Inset: optical band gap from UV-Visible spectroscopic measurement of $CuMnO_2$ and $CuMn_{0.95}Fe_{0.05}O_2$.

Fig. 7 Variation of resistivity versus temperature for $CuMn_{1-x}Fe_xO_2$ (where $x = 0$, 0.05). Inset variation of ln ρ vs. 1000/T for ($x = 0$ and 0.05) samples.
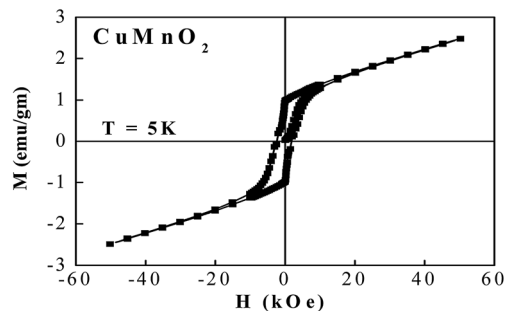
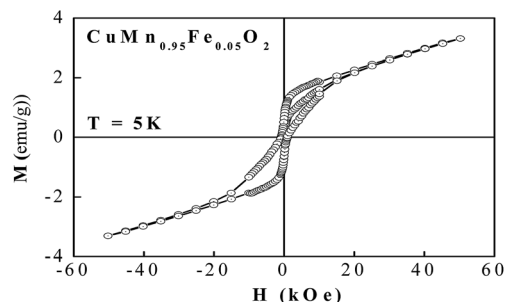**Fig. 8** Magnetization curve $M(H)$ of $CuMnO_2$ at 5 K.

Fig. 9 Magnetization curve $M(H)$ of $CuMn_{0.95}Fe_{0.05}O_2$ at 5 K.

ordering at 50 K has also been reported recently by Kurakawa *et al.*[28] The increase of high field magnetization along with the appearance of H_c indicates the emergence of an uncompensated moment. When Fe is doped (Fig. 9), the magnetization is increased but the coercivity is decreased. With increase of the magnetic field the ferromagnetic correlation precipitates and the antiferromagnetic correlation is increased which is clear from the $M(H)$ curve. The change in magnetic behavior with Fe doping can be explained in terms of magnetic exchanges, direct Mn–Mn interactions may be considered as dominant in-plane but indirect exchanges (*via* oxygen) could also play a role, all Mn–O–Mn angles being close to 90°. The super–super exchange, along Mn–O–Cu–O–Mn path ways, may also play the role for the 3D magnetic ordering. In fact super–super exchange *via* diamagnetic cation is quite common, as is observed in different oxides.[11] The difference in magnetic behavior with Fe doping might be due to the presence of $k_2 = (1/2 \cdot 1/2 \cdot 0)$ vector which has been observed from neutron diffraction measurement. As has been mentioned that the appearance of $k_2 = (1/2 \cdot 1/2 \cdot 0)$ vector is the indication of ferromagnetic coupling between *ab* planes implying that Fe doping induces this ferromagnetic coupling. Similar behavior is observed in the non-stoichiometric $Cu_{1.04}Mn_{0.96}O_2$.[10]

Conclusion

Neutron diffraction, synchrotron X-ray diffraction, XPS, magnetic and UV-Visible spectroscopic measurements have been investigated on $CuMnO_2$ and 5% Fe doped $CuMnO_2$ samples, with assumption that these measurements have complementary information on structural and magnetic behaviour of the samples. On Fe doping, the apical Mn–O distances decrease while the equatorial distances slightly increase, reducing the distortion in MnO_6 octahedra. Moreover, when Fe is doped along with $k_1 = (1/2 \cdot 1/2 \cdot 1/2)$ the magnetic peaks can also be indexed with the propagation vector $k_2 = (1/2 \cdot 1/2 \cdot 0)$ indicating the appearance of ferromagnetic coupling between *ab* planes. Value of magnetization is increased with Fe doping but coercivity is decreased. These might be due to direct Mn–Mn exchange and Mn–O–Cu–O–Mn super–super exchange interactions. The UV-Vis data showed the increase in one of the two energy gaps, on Fe doping, indicating the usefulness of these materials as wide band gap magnetic semiconductors.

Acknowledgements

References

1 T. Kimura, T. Goto, H. Shintani, K. Ishizaka, T. Arima and Y. Tokura, Magnetic control of ferroelectric polarization, *Nature*, 2003, **426**, 55–58.

2 N. Hur, S. Park, P. A. Sharma, J. S. Ahn, S. Guha and S. W. Cheong, Electric polarization reversal and memory in a multiferroic material induced by magnetic fields, *Nature*, 2004, **429**, 392–395.

3 T. Lottermoser, T. Lonkai, U. Amann, D. Hohlwein, J. Ihringer and M. Fiebig, Magnetic phase control by an electric field, *Nature*, 2004, **430**, 541–544.

4 A. J. W. Reitsma, L. F. Feiner and A. M. Oles, Orbital and spin physics in $LiNiO_2$ and $NaNiO_2$, *New J. Phys.*, 2005, **7**, 121.

5 F. Ye, J. A. Fernandez-Baca, R. S. Fishman, Y. Ren, H. J. Kang, Y. Qiu and T. Kimura, Magnetic Interactions in the Geometrically Frustrated Triangular Lattice Antiferromagnet $CuFeO_2$, *Phys. Rev. Lett.*, 2007, **99**, 157201.

6 D. J. Singh, Magnetic and electronic properties of $LiMnO_2$, *Phys. Rev. B: Condens. Matter Mater. Phys.*, 1997, **55**, 309–312.

7 T. Jia, G. Guo Zhang and Z. Zeng, Orbitally relieved magnetic frustration in $NaVO_2$, *Phys. Rev. B: Condens. Matter Mater. Phys.*, 2009, **80**, 045103.

8 F. Damay, M. Poienar, C. Martin, A. Maignan, J. Rodriguez-Carvajal, G. Andre and J. P. Doumerc, Spin-lattice coupling induced phase transition in the $S = 2$ frustrated antiferromagnet $CuMnO_2$, *Phys. Rev. B: Condens. Matter Mater. Phys.*, 2009, **80**, 094410.

9 A. V. Ushakov, S. V. Streltsov and D. I. Khomskii, Orbital structure and magnetic ordering in stoichiometric and doped crednerite $CuMnO_2$, *Phys. Rev. B: Condens. Matter Mater. Phys.*, 2009, **80**, 094410.

10 M. Poienar, C. Vecchini, G. Andre, A. Daoud-Aladine, I. Margiolaki, A. Maignan, A. Lappas, L. Chapon, M. Hervieu, F. Damay and C. Martin, Substitution Effect

on the Interplane Coupling in Crednerite: the $Cu_{1.04}Mn_{0.96}O_2$ Case, *Chem. Mater.*, 2011, **23**, 85–94.

11 C. Vecchini, M. Poienar, F. Damay, O. Adamopoulos, A. Daoud-Aladine, A. Lappas, J. M. Perez-Mato, L. C. Chapon and C. Martin, Magnetoelastic coupling in the frustrated antiferromagnetic triangular lattice $CuMnO_2$, *Phys. Rev. B: Condens. Matter Mater. Phys.*, 2010, **82**, 094404.

12 M. Trari, J. Topfer, P. Dordor, J. C. Grenier, M. Pouchard and J. P. Doumerc, Preparation and physical properties of the solid solutions $Cu_{1+x}Mn_{1-x}O_2$ ($0 \leq x \leq 0.2$), *J. Solid State Chem.*, 2005, **178**, 2751–2758.

13 J. Topfer, M. Trari, P. Garavcreau, J. P. Chaminade and J. P. Z. Doumerc, *Kristallografiya*, 1995, **210**, 184.

14 I. D. Kandrashev, *Sov. Phys. Crystallogr.*, 1959, **3**, 703.

15 V. Ovidiu Garlea, A. T. Savici and R. Jin, Tuning the magnetic ground state of a triangular lattice system $Cu(Mn_{1-x}Cu_x)O_2$, *Phys. Rev. B: Condens. Matter Mater. Phys.*, 2011, **83**, 172407.

16 Y. Shirako, H. Satsukawa, X. X. Wang, J. J. Li, Y. F. Guo, M. Arai, K. Yamaura, M. Yoshida, H. Kojitani, T. Katsumata, Y. Inaguma, K. Hiraki, T. Takahashi and M. Akaogi, Integer spin-chain antiferromagnetism of the 4d oxide $CaRuO_3$ with post-perovskite structure, *Phys. Rev. B: Condens. Matter Mater. Phys.*, 2011, **83**, 17441.

17 G. Gusmano, G. Montesperelli, E. Traversa and G. Mattogno, Microstructure and electrical properties of $MgAl_2O_4$ thin films for humidity sensing, *J. Am. Ceram. Soc.*, 1993, **76**, 743–750.

18 D. Shin, J. S. Foord, D. J. Payne, T. Arnold, D. J. Aston, R. G. Egdell, K. G. Godinho, D. O. Scanlon, B. J. Morgan, G. W. Watson, E. Mugnier, C. Yaicle, A. Rougier, L. Colakerol, P. A. Glans, L. F. J. Piper and K. E. Smith, Comparative study of bandwidths in copper delafossites from x-ray emission spectroscopy, *Phys. Rev. B: Condens. Matter Mater. Phys.*, 2009, **80**, 233105.

19 T. Arnold, D. J. Payne, A. Bourlange, J. P. Hu, R. G. Egdell, L. F. J. Piper, L. Colakerol, A. D. Masi, P. A. Glans, T. Learmonth, K. E. Smith, D. O. Scanlon, A. Walsh, B. J. Morgan and G. W. Watson, X-ray spectroscopic study of the electronic structure of $CuCrO_2$, *Phys. Rev. B: Condens. Matter Mater. Phys.*, 2009, **79**, 075102.

20 C. C. B. Lynch, R. G. Egdell and D. S. L. Law, High resolution X-ray photoemission of $SrCu_2O_2$, *Chem. Phys. Lett.*, 2005, **401**, 223–226.

21 M. Han, K. Jiang, J. Zhang, W. Yu, Y. Li, Z. Hu and J. Chu, Structural, electronic band transition and optoelectronic properties of delafossite $CuGa_{1-x}Cr_xO_2$ ($0 \leq x \leq 1$) solid solution films grown by the sol–gel method, *J. Mater. Chem.*, 2012, **22**, 18463–18470.

22 A. Mang, K. Reimann and S. Rubenacke, Band gaps, crystal-field splitting, spin–orbit coupling, and exciton binding energies in ZnO under hydrostatic pressure, *Solid State Commun.*, 1995, **94**, 251–254.

23 O. Madelung, *Semiconductor basic data 2nd review edition*, Springer, Berlin, 1996.

24 S. Kumar, S. Chatterjee, K. K. Chattopadhyay and A. K. Ghosh, Sol–gel derived ZnO: Mn nanocrystals: study of structural, Raman and optical properties, *J. Phys. Chem. C*, 2012, **116**, 16700–16708.

25 N. F. Mott, Conduction in glasses containing transition metal ions, *J. Non-Cryst. Solids*, 1968, **1**, 1–17.

26 J. P. Doumerc, M. Trari, J. Topfer, L. Fournes, J. C. Greinier, M. Pouchard and P. Hagenmuller, Magnetic properties of the crednerite $CuMnO_2$, *Eur. J. Solid State Inorg. Chem.*, 1994, **31**, 705–715.

27 Y. Bessekhouad, Y. Gabes, A. Bouguelia and M. Trari, The physical and photo electrochemical characterization of the crednerite $CuMnO_2$, *J. Mater. Sci.*, 2007, **42**, 6469–6476.

28 A. Kurakawa, T. Yanoh, S. Yano and Y. Ichiyanagi, Preparation and Magnetic Properties of Multiferroic $CuMnO_2$ Nanoparticles, *J. Nanosci. Nanotechnol.*, 2014, **14**, 2553–2556.